

## HYDRODYNAMIC SIMULATIONS OF COUNTERROTATING ACCRETION DISKS

O. A. KUZNETSOV

Keldysh Institute of Applied Mathematics, Russian Academy of Sciences, Moscow, Russia; kuznecov@spp.keldysh.ru

R. V. E. LOVELACE

Department of Astronomy, Cornell University, Ithaca, NY 14853-6801; rv11@cornell.edu

M. M. ROMANOVA

Space Research Institute, Russian Academy of Sciences, Moscow, Russia; and Department of Astronomy, Cornell University, Ithaca, NY 14853-6801; romanova@astrosun.tn.cornell.edu

AND

V. M. CHECHETKIN

Keldysh Institute of Applied Mathematics, Russian Academy of Sciences, Moscow, Russia; chech@int.keldysh.ru

Received 1998 February 24; accepted 1998 November 3

### ABSTRACT

Time-dependent, axisymmetric hydrodynamic simulations have been used to study accretion disks consisting of counterrotating components with an intervening shear layer(s). Configurations of this type can arise from the accretion of newly supplied counterrotating matter onto an existing corotating disk. The grid-dependent numerical viscosity of our hydrocode is used to simulate the influence of a turbulent viscosity of the disk. First, we consider the case where the gas well above the disk midplane ( $z > 0$ ) rotates with angular rate  $+\Omega(r)$  and that well below ( $z < 0$ ) has the same properties but rotates with rate  $-\Omega(r)$ . We find that there is angular momentum annihilation in a narrow equatorial boundary layer in which matter accretes supersonically with a velocity that approaches the free-fall velocity. This is in accord with the recent analytic model of Lovelace & Chou. The average accretion speed of the disk can be enormously larger than that for a conventional  $\alpha$ -disk rotating in one direction. Under some conditions the interface between the corotating and counterrotating components shows significant warping. Second, we consider the case of a corotating accretion disk for  $r < r_t$  and a counterrotating disk for  $r > r_t$ . In this case we observed, that matter from the annihilation layer lost its stability and propagated inward, pushing matter of inner regions of the disk to accrete. Third, we investigated the case where counterrotating matter inflowing from large radial distances encounters an existing corotating disk. Friction between the inflowing matter and the existing disk is found to lead to fast boundary layer accretion along the disk surfaces and to enhanced accretion in the main disk.

These models are pertinent to the formation of counterrotating disks in galaxies and possibly in active galactic nuclei and in X-ray pulsars in binary systems. For galaxies, the high accretion speed allows counterrotating gas to be transported into the central regions of a galaxy in a time much less than the Hubble time.

*Subject headings:* accretion, accretion disks — galaxies: evolution — galaxies: formation — galaxies: nuclei — galaxies: spiral — hydrodynamics

### 1. INTRODUCTION

The widely considered models of accretion disks have gas rotating in one direction with a turbulent viscosity acting to transport angular momentum outward (Shakura 1973; Shakura & Sunyaev 1973). However, recent observations indicate that there may be more complicated disk structures in some cases on a galactic scale, in galactic nuclei, and in disks around compact stellar-mass objects. Studies of normal galaxies have revealed counterrotating gas and/or stars in many galaxies of all morphological types—elliptical, spiral, and irregular (Rubin 1994a, 1994b; Galletta 1995). In elliptical galaxies, the counterrotating component is usually in the nuclear core and may result from the merging of galaxies with opposite angular momentum.

In a number of spirals and S0 galaxies, counterrotating disks of stars and/or gas have been found to coexist with the primary disk out to large distances (10–20 kpc), with the first example, NGC 4550, discovered by Rubin, Graham, & Kenney (1992). Of interest here is the “Evil Eye” galaxy NGC 4826, in which the direction of rotation of the gas reverses going from the inner ( $180 \text{ km s}^{-1}$ ) to the outer disk ( $-200 \text{ km s}^{-1}$ ) with an inward radial accretion speed of

more than  $100 \text{ km s}^{-1}$  in the transition zone, whereas the stars at all radii rotate in the same direction as the gas in the inner disk, which has a radius  $\sim 1200 \text{ pc}$  (Braun et al. 1994; Rubin 1994a, 1994b). The large-scale counterrotating disks probably do not result from mergers of flat galaxies with opposite spins because of the large vertical thickening observed in simulation studies of such mergers (Hernquist & Barnes 1991; Barnes 1992). Thakar & Ryden (1996) discuss different possibilities: (1) that the counterrotating matter comes from the merger of an oppositely rotating gas-rich dwarf galaxy with an existing spiral and (2) that the accretion of gas occurs over the lifetime of the galaxy with the more recently accreted gas counterrotating. Subsequent star formation in the counterrotating gas may then lead to counterrotating stars. Counterrotating gas may have a strong interaction with the gas resulting from mass loss by corotating stars (Braun et al. 1994). Furthermore, the two-stream instability between counterrotating gas and corotating stars can be important for gas accretion (Lovelace, Jore, & Haynes 1997).

Accretion of counterrotating matter onto an existing corotating disk around a massive black hole may occur in

an active galactic nucleus (AGN). The counterrotating matter may come from recently captured material from a galaxy merger, from a tidally disrupted molecular cloud, or from a star. Tidal disruption of a star by the central black hole may release essential part of the star in the form of gas (Rees 1990; Shlosman, Begelman, & Frank 1990; Khokhlov & Melia 1996). There is a significant probability that this gas has angular momentum opposite to that of the main disk. This can lead to formation of small disks with opposite angular momentum in the center of a galaxy (Melia 1994). This was studied using three-dimensional numerical simulations by Ruffert (1994) and Ruffert & Melia (1994). The retrograde disks may also slow down the rotation of the central black hole (Moderski & Sikora 1996). The greatly enhanced accretion rate for counterrotating matter in the presence of a corotating disk may give outbursts of AGNs.

Another situation where counterrotating matter may encounter an existing corotating disk is in low-mass X-ray binary sources where the accreting, magnetized rotating neutron stars are observed to jump between states where they spin up and those where they spin down. Nelson et al. (1997a, 1997b) and Chakrabarty et al. (1997) have proposed that the change from spin-up to spin-down results from a reversal of the angular momentum of the wind-supplied accreting matter. Their suggestion is based on the recent *BATSE* observations that show a rapid change from spin-up to spin-down evolution of some X-ray pulsars. This is difficult to explain with conventional theory (see, however, Lovelace, Romanova, & Bisnovatyi-Kogan 1998). Reversal of the angular momentum of accreted matter in wind-fed binaries was observed in the two-dimensional simulations by Blondin et al. (1990), Livio et al. (1991), and Bisikalo et al. (1996).

An important open problem is to understand the *hydrodynamic* interaction of counterrotating gaseous disks. Earlier two-dimensional simulations used either collisionless particles to represent a system of stars (Davies & Hunter 1997) or “sticky” particles (Thakar & Ryden 1996 and references therein) to represent a system of clouds. The sticky particle interaction gives only a rough representation of a viscous fluid. When both components of a counterrotating system are gaseous, it is important to understand their interaction using the full equations of hydrodynamics including the viscous transport of angular momentum. Hydrodynamic interaction of a galactic disk with infalling matter of a nonrotating corona was investigated by Falcke & Melia (1997) using a one-dimensional approach. They showed that this interaction may lead to significant evolution of the disk.

Lovelace & Chou (1996, hereafter LC) developed an analytic theory of the viscous hydrodynamic interaction of counterrotating gaseous disks basing on the  $\alpha$ -viscosity model of Shakura (1973) and Shakura & Sunyaev (1973).

Here we present the results of two-dimensional, time-dependent hydrodynamic simulations of counterrotating accretion disks. We investigate three main models, which are sketched in Figure 1.

1. Model I (Fig. 1, *top panel*): In this case the accretion disk consists of counterrotating gaseous components with gas above the disk midplane rotating with angular rate  $+\Omega(r)$  and that below rotating at rate  $-\Omega(r)$ . The interface between the components at  $z \sim 0$  constitutes a supersonic shear layer. A configuration of this type may

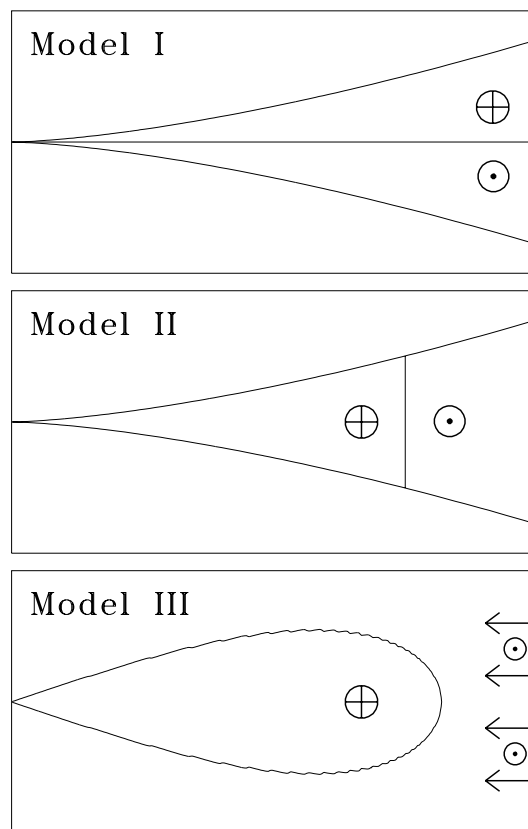


FIG. 1.—Sketches of three main cases considered in this paper. The (circled plus sign,  $\oplus$ ) indicates corotating matter and (circled dot,  $\odot$ ) counterrotating matter. Details of the models are described in the text.

arise from the accretion of newly supplied counterrotating gas onto an existing corotating disk. For this case, the analytical model of Lovelace & Chou (1996) proposed that matter approaching the equatorial plane from above and below has angular momenta of opposite signs, with the result that there is angular momentum annihilation at  $z \sim 0$ . This matter loses its centrifugal support and accretes at essentially free-fall speed.

2. Model II (Fig. 1, *middle panel*): In this model we consider the case where there is a corotating ( $+\Omega$ ) accretion disk (the “old” disk) for  $r < r_i$  and a counterrotating ( $-\Omega$ ) disk (the “new” disk) in the region  $r > r_i$ . This case is clearly pertinent to the “Evil Eye” galaxy NGC 4826.

3. Model III (Fig. 1, *bottom panel*): This model corresponds to inflow of counterrotating matter that interacts with an existing corotating disk. In this case, the annihilation of angular momentum occurs on the surface of the existing disk, and this can lead to fast accretion.

In § 2 we discuss the pertinent fluid dynamical equations for axisymmetric accretion, the initial and boundary conditions, and the numerical method used. In §§ 3–5 we discuss results obtained for models I–III. We present astrophysical examples in § 6. In § 7 we give conclusions of this work.

## 2. MATHEMATICAL MODEL

### 2.1. Basic Equations

The axisymmetric flows are described by the inviscid hydrodynamic equations (Euler equations) in spherical,

inertial coordinates  $(R, \phi, \theta)$  (with  $\theta = 0$  the equatorial plane):

$$\frac{\partial \rho}{\partial t} + \frac{1}{R^2} \frac{\partial}{\partial R} (R^2 \rho v_R) + \frac{1}{R \cos \theta} \frac{\partial}{\partial \theta} (\cos \theta \rho v_\theta) = 0, \quad (1a)$$

$$\begin{aligned} \frac{\partial(\rho v_R)}{\partial t} + \frac{1}{R^2} \frac{\partial}{\partial R} [R^2(\rho v_R^2 + p)] + \frac{1}{R \cos \theta} \frac{\partial}{\partial \theta} (\cos \theta \rho v_R v_\theta) \\ = \frac{2p}{R} - \rho \frac{\partial \Phi_g}{\partial R} + \rho \frac{v_\phi^2 + v_\theta^2}{R}, \end{aligned} \quad (1b)$$

$$\begin{aligned} \frac{\partial[\rho(R \cos \theta v_\phi)]}{\partial t} + \frac{1}{R^2} \frac{\partial}{\partial R} [R^2 \rho (R \cos \theta v_\phi) v_R] \\ + \frac{1}{R \cos \theta} \frac{\partial}{\partial \theta} [\cos \theta \rho (R \cos \theta v_\phi) v_\theta] = 0, \end{aligned} \quad (1c)$$

$$\begin{aligned} \frac{\partial(\rho v_\theta)}{\partial t} + \frac{1}{R^2} \frac{\partial}{\partial R} (R^2 \rho v_\theta v_R) + \frac{1}{R \cos \theta} \frac{\partial}{\partial \theta} [\cos \theta (\rho v_\theta^2 + p)] \\ = -\frac{p \tan \theta}{R} - \rho \frac{v_R v_\theta}{R} - \rho \frac{v_\phi^2}{R} \tan \theta, \end{aligned} \quad (1d)$$

$$\begin{aligned} \frac{\partial(\rho \mathcal{E})}{\partial t} + \frac{1}{R^2} \frac{\partial}{\partial R} (R^2 \rho \tilde{w} v_R) + \frac{1}{R \cos \theta} \frac{\partial}{\partial \theta} (\cos \theta \rho \tilde{w} v_\theta) \\ = -\rho \frac{\partial \Phi_g}{\partial R} v_R. \end{aligned} \quad (1e)$$

Here  $\rho(R, \theta)$  is the density;  $v(R, \theta)$  the flow velocity, with components  $(v_R, v_\phi, v_\theta)$ ;  $p(R, \theta)$  the pressure;  $\Phi_g$  the gravitational potential;  $\mathcal{E}$  the full specific energy  $\mathcal{E} \equiv \epsilon + (v_R^2 + v_\phi^2 + v_\theta^2)/2$ ;  $\epsilon$  the specific internal energy; and  $\tilde{w}$  the full specific enthalpy,  $\tilde{w} \equiv \epsilon + p/\rho + (v_R^2 + v_\phi^2 + v_\theta^2)/2$ . An equation of state is necessary, and we assume the ideal gas equation,

$$p = (\gamma - 1)\epsilon \rho,$$

where  $\gamma$  is the usual ratio of heat capacities. The gravitational potential is considered to be the Newtonian potential of the central object:

$$\Phi_g = -\frac{GM}{R}.$$

That is, we assume that the self-gravity of the disk is negligible.

## 2.2. Alternative Form of Energy Equation

In our early disk simulations we found that the energy equation taken in divergent form (eq. [1e]) can lead to inaccurate results. The reason for this is the large value of the azimuthal velocity  $v_\phi$  and the corresponding kinetic energy  $v_\phi^2/2$  in comparison with other velocities/energies. The relatively small quantity  $\epsilon$  is determined from equation (1e) inaccurately in this case.

To correct this problem we now have excluded the  $\phi$ -velocity part of the energy from the energy equation by writing

$$\begin{aligned} \frac{\partial}{\partial t} \left( \rho \frac{v_\phi^2}{2} \right) + \frac{1}{R^2} \frac{\partial}{\partial R} \left( R^2 \rho \frac{v_\phi^2}{2} v_R \right) + \frac{1}{R \cos \theta} \\ \times \frac{\partial}{\partial \theta} \left( \cos \theta \rho \frac{v_\phi^2}{2} v_\theta \right) = -\rho \frac{v_\phi^2 v_R}{R} + \rho \frac{v_\phi^2 v_\theta}{R} \tan \theta, \end{aligned}$$

and subtracting this equation from equation (1e) to obtain another divergent form of energy equation,

$$\begin{aligned} \frac{\partial}{\partial t} (\rho \mathcal{E}') + \frac{1}{R^2} \frac{\partial}{\partial R} (R^2 \rho \tilde{w}' v_R) + \frac{1}{R \cos \theta} \frac{\partial}{\partial \theta} (\cos \theta \rho \tilde{w}' v_\theta) \\ = -\rho \frac{\partial \Phi_g}{\partial R} v_R + \rho \frac{v_\phi^2 v_R}{R} - \rho \frac{v_\phi^2 v_\theta}{R} \tan \theta, \end{aligned} \quad (2)$$

where  $\mathcal{E}'$  and  $\tilde{w}'$  are the “reduced” (poloidal) full specific energy and the “reduced” (poloidal) full specific enthalpy,  $\mathcal{E}' \equiv \epsilon + (v_R^2 + v_\theta^2)/2$  and  $\tilde{w}' \equiv \epsilon + p/\rho + (v_R^2 + v_\theta^2)/2$ , respectively. In all of our calculations, equation (2) was used instead of equation (1e).

## 2.3. Characteristic Scales

The physical quantities have evident characteristic scales: distances are measured in terms of the inner radius of the disk  $R_0$ . Velocities are measured in terms of the Keplerian velocity at the inner edge of the disk,  $V_{K0} \equiv \sqrt{GM/R_0}$ . Time is measured in units of the period of revolution of the inner edge of the disk  $t_0 \equiv 2\pi R_0/V_{K0}$ . The density is given in relative units.

## 2.4. Initial Equilibria

We have adopted spherical coordinates for our simulations in order to obtain a good match of the grid to the accretion disk that in general has a thickness in the  $z$ -direction ( $2H$ ) increasing with  $R$ . However, for convenience our figures and initial disk equilibria described in this subsection are given in  $(r, z)$  coordinates.

### 2.4.1. Initial Conditions 1

A disk equilibrium with  $v_r = 0$ ,  $v_z = 0$ , but  $v_\phi \neq 0$  is described by the equations

$$\frac{1}{\rho} \frac{\partial p}{\partial r} = \frac{v_\phi^2}{r} - \frac{\partial \Phi_g}{\partial r}, \quad (3a)$$

$$\frac{1}{\rho} \frac{\partial p}{\partial z} = -\frac{\partial \Phi_g}{\partial z}, \quad (3b)$$

where the position and velocity are now dimensionless, as mentioned.

With the assumption of a polytropic gas  $p = K\rho^{1+1/n}$ , where  $n$  is the polytropic index,  $n \equiv 1/(\gamma - 1)$ , the common solution of equations (3a) and (3b) can be written as

$$w = w_0 + F - \Phi_g = w_0 + F + \frac{1}{\sqrt{r^2 + z^2}}, \quad (4)$$

where  $w$  is the specific enthalpy,  $w = K(n+1)\rho^{1/n} = nc_s^2$ , with  $w_0$  a constant,  $c_s = \sqrt{\gamma p/\rho}$  the sound speed, and  $F(r)$  an arbitrary function depending only on  $r$ . The azimuthal velocity  $v_\phi$  is given in this case as

$$v_\phi^2 = r \frac{\partial F}{\partial r}.$$

The disk boundary is determined by the condition  $w = 0$  or  $\rho = 0$ . If we assume the Keplerian law for azimuthal velocity,  $v_\phi^2 = 1/r$ , then

$$F = -\frac{1}{r} = \Phi_g(r, z = 0),$$

and

$$\rho = \rho_0 \left\{ 1 - \frac{(1/r) - [1/(r^2 + z^2)^{1/2}]}{nc_{s0}^2} \right\}^n, \quad (5)$$

where  $\rho_0$  and  $c_{s0}$  are the values at the point ( $r = 1, z = 0$ ). The disk boundary in this case is

$$z^2 = \frac{r^2}{1 - nc_{s0}^2 r^2} - r^2,$$

so the disk thickness diverges at some very large radius outside the region of interest. A sample density distribution is shown in Figure 2. Hereafter, we refer to this case as “Initial Conditions 1.” This was used for the runs described in §§ 3 and 4.

#### 2.4.2. Initial Conditions 2

A second equilibrium disk model was used in our simulations. For this we took the disk boundary ( $\rho = 0$ ) to have the form

$$z^2 = r^2 \left( 1 - \frac{r^2}{r_1^2} \right) \Delta^2,$$

where  $r_1$  and  $\Delta$  are parameter determining disk radial size and thickness. The rotation (slightly sub-Keplerian), enthalpy, and density for this case are

$$v_\phi^2 = \frac{1}{r\sqrt{1 + \Delta^2}} \frac{1 - (2r^2/r_1^2)\beta}{[1 - (r^2/r_1^2)\beta]^{3/2}}, \quad (6a)$$

$$w = \frac{1}{\sqrt{r^2 + z^2}} - \frac{1}{r\sqrt{1 + \Delta^2 - (r^2/r_1^2)\Delta^2}}, \quad (6b)$$

$$\rho = \rho_0 w^n, \quad \beta = \frac{\Delta^2}{1 + \Delta^2}. \quad (6c)$$

The density distribution for this case is shown in Figure 3. Hereafter, we refer to this case as “Initial Conditions 2.”

For building equilibria we have used both a rotation law based approach and one based on the shape of the disk surface. For the first case, the equilibria are found for known rotation law according to the chain  $v_\phi(r) \mapsto F(r) \mapsto w(r, z) \mapsto z(r)|_{\rho=0}$ . For the second case, a known disk surface is used according to the chain  $z(r)|_{\rho=0} \mapsto F(r) = \Phi[r, z(r)] - w_0 \mapsto v_\phi(r)$ . Abakumov et al. (1996) use an analogous approach.

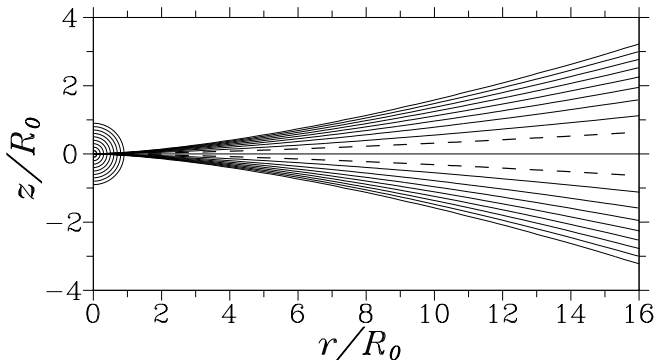


FIG. 2.—Log-scaled isodensity lines from  $\rho_{\min} = 10^{-6}$  to  $\rho_{\max} = 1$  for a Keplerian disk described in § 2.4.1 with  $c_{s0} = 0.01$  and  $\gamma = 1.01$ . The dashed lines show the standard disk scale height,  $H = rc_s/V_K$ . The circles represent the region  $r^2 + z^2 \leq R_0^2$ , where matter is considered to be absorbed.

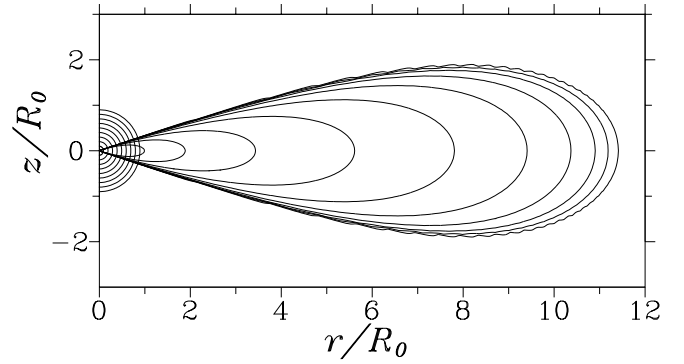


FIG. 3.—Log-scaled isodensity lines from  $\rho_{\min} = 10^{-6}$  to  $\rho_{\max} = 1$  for a sub-Keplerian disk as described in § 2.4.2 for  $\Delta = 1/3$ ,  $r_1 = 11.5R_0$ , and  $n = 3/2$  (or  $\gamma = 5/3$ ).

#### 2.5. Boundary Conditions

Simulations were performed in the region  $R_0 \leq R \leq R_{\max}$ ,  $-\pi/2 \leq \theta \leq \pi/2$ .

The outer boundary conditions  $R = R_{\max}$  are treated following the method used by Sawada based on the solution of the Riemann problem (see, e.g., Sawada, Matsuda, & Hachisu 1986; Sawada & Matsuda 1992). These boundary conditions were used for models I and II. However, for model III different boundary conditions are applied in that matter is considered to inflow supersonically through part of the outer boundary.

We assume that all matter coming into the sphere  $R \leq R_0$  is absorbed. On the  $z$ -axis,  $\theta = \pm\pi/2$ , we of course have  $v_\theta = 0$  and  $v_\phi = 0$ .

No symmetry is assumed with respect to the equatorial plane.

#### 2.6. Numerical Method and Viscosity Treatment

An explicit Lax-Friedrichs finite-difference scheme with flux correction in Chakravarthy-Osher (Chakravarthy & Osher 1985) form was used. This scheme is first order of approximation in time and third order of approximation in space and is oscillation-free near discontinuities. The combined Lax-Friedrichs-Osher scheme was suggested in work by Vyaznikov, Tishkin, & Favorsky (1989).

Figure 4 shows the nonhomogeneous  $(R, \theta)$  grid used in the simulations. The radial grid increment  $\delta R$  increases outward exponentially,  $\delta R = \delta R_0 a^{R/R_0}$ , where  $a = 1.05$ . The  $\theta$ -grid  $\delta\theta$  increases in a similar way going away from the equatorial plane. For a disk that has thickness  $h$  increasing with  $r$ , this type of grid gives a more uniform distribution of cells within the disk including its central regions. In the simulations we used grids of  $N_R \times N_\theta$  of  $100 \times 100$  or  $200 \times 200$  in some cases.

The simulation method used naturally has numerical viscosity. With a fixed grid, we cannot vary the numerical viscosity, but we can investigate its influence. The coefficient of numerical viscosity can be represented as  $\nu_{\text{num}} \sim c_s \Delta h$ , where  $c_s$  is the sound speed and  $\Delta h$  is the size of the grid. This expression for  $\nu$  is analogous to that proposed by Shakura (1973) and Shakura & Sunyaev (1973) for the turbulent viscosity of accretion disks,  $\nu = \alpha c_s H$ , where  $H$  is the thickness of the disk and  $\alpha \sim 10^{-1} - 10^{-3}$  is a dimensionless parameter. We calculated the steady accretion for a disk rotating in one direction and observed the accretion due to

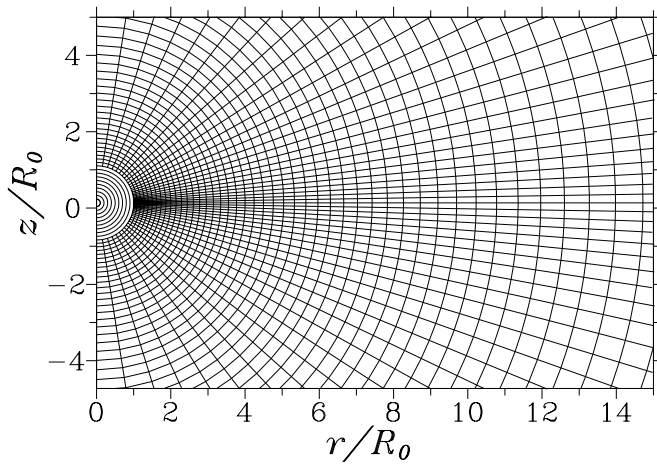


FIG. 4.—Example of nature of grid used in simulations. The grid is in spherical coordinates with  $R$  the radial distance and  $\theta$  the colatitude measured from the equatorial plane. The grid is nonhomogeneous with increments increasing exponentially with both  $R$  and  $|\theta|$ . The grid shown has  $N_R \times N_\theta = 50 \times 50$ .

the numerical viscosity. Using the formula for the accretion speed of a viscous accretion disk,  $v_r \sim \nu/r$ , we estimated that  $\alpha < 1$  for  $r > 5R_0$  for a  $200 \times 200$  grid and  $\alpha < 1$  for  $r > 7R_0$  for a  $100 \times 100$  grid, and  $\alpha$  decreases to  $\alpha \sim 0.03$ – $0.1$  at the outer radii. A challenge for future work is the inclusion of a true  $\alpha$ -viscosity.

We investigated three different models of counterrotating accretion flows that correspond to different possible astrophysical situations. The first model corresponds to disks counterrotating in the  $z$ -direction (model I, § 3). The second corresponds to disks counterrotating in the  $r$ -direction (model II, § 4). The third corresponds to counterrotating gas infalling onto a preexisting corotating disk (model III, § 5).

### 3. DISK COUNTERROTATING IN THE $z$ -DIRECTION: MODEL I

Here we discuss simulation results for model I where initially the upper half of the disk ( $z > 0$ ) is corotating ( $+\Omega_K$ ) while the lower half ( $z < 0$ ) is counterrotating ( $-\Omega_K$ ). This case was treated analytically by LC, and therefore we have a test both of the LC theory and of our simulation code.

First, in § 3.1, we check the initial equilibrium disk for the conventional case of unidirectional disk rotation. Second, in § 3.2, we investigate the counterrotating disk for  $\gamma = 1.01$ , which is close to isothermal. This value of  $\gamma$  close to unity mimics conditions of strong radiative cooling. In this subsection we compare the simulation results with the predictions of LC where radiative cooling is included. In this subsection we used a  $100 \times 100$  grid. Third, in § 3.3, we discuss the cases  $\gamma = 1.1$  and  $5/3$ , which correspond to non-isothermal conditions where numerical viscous heating is significant. In this subsection we used a  $200 \times 200$  grid.

#### 3.1. Conventional Accretion Disk

As a calibration of our simulation code, we investigated a conventional accretion disk that rotates in only one direction. The disk evolves as a result of the relatively small numerical viscosity of the code. We took Initial Conditions 1 (see § 2.4.1) with  $\gamma = 1.01$  and performed long-term numerical simulations of this disk. We observed that the

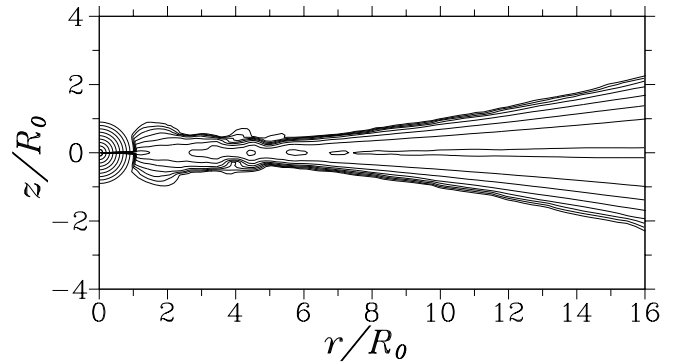


FIG. 5.—Isodensity lines for a conventional disk rotating in one direction for Initial Conditions 1 after a time  $t = 40t_0$ , where  $t_0$  is the period of rotation of the inner edge of the disk at  $r = R_0$ . The disk is close to its initial configuration, excluding the inner part, which has changed as a result of numerical viscosity. Simulations were performed with a  $100 \times 100$  grid.

disk shape did not change during many periods of rotation of the inner radius of the disk. Figure 5 shows the isodensity contours distribution at  $t = 40t_0$ . The evolved disk is close to that at  $t = 0$  (see Fig. 2), excluding the inner part, where the thickness of the disk is very small (comparable with the grid size), and the numerical viscosity has a noticeable influence.

#### 3.2. $\gamma = 1.01$

This case is close to isothermal and is closest to the LC analytical model where both viscous heating and radiative cooling are included.

We took Initial Conditions 1 for the initial conditions for the density and velocity of the disk (see Fig. 2), but put the angular velocity in the lower half of the disk ( $z < 0$ ) opposite to the angular velocity of the upper half ( $z > 0$ ). Figure 6 shows that matter starts to rapidly flow radially inward in a narrow region near the midplane of the disk. The poloidal flow near the midplane is supersonic, and the radial inflow velocity increases as  $r$  decreases.

Figure 7 shows the radial variation of the radial velocity in the midplane of the disk at different times. The velocity distribution changes only gradually with time. The velocity close to the gravitating center,  $r/R_0 \sim 1$ – $3$ , is much larger than velocity in the outer regions of the disk,  $r/R_0 \sim 16$ – $18$ .

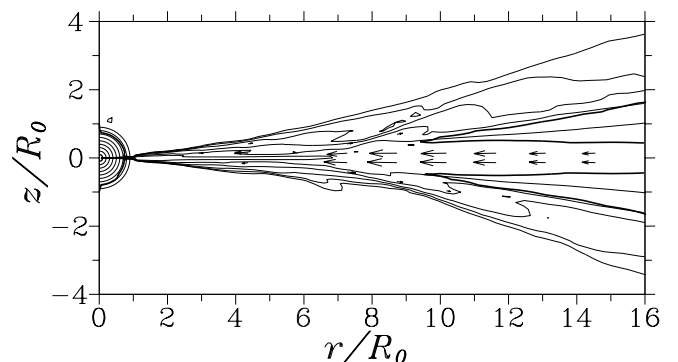


FIG. 6.—Isodensity contours (solid lines) and mass flux vectors ( $\rho v$ ) in counterrotating accretion disk at time  $t = 14t_0$ , where  $t_0$  is the rotation period at the inner radius of the disk. The poloidal flow near the midplane of the disk is supersonic, excluding the small regions separated by the heavy lines. Simulations were performed with a  $100 \times 100$  grid.

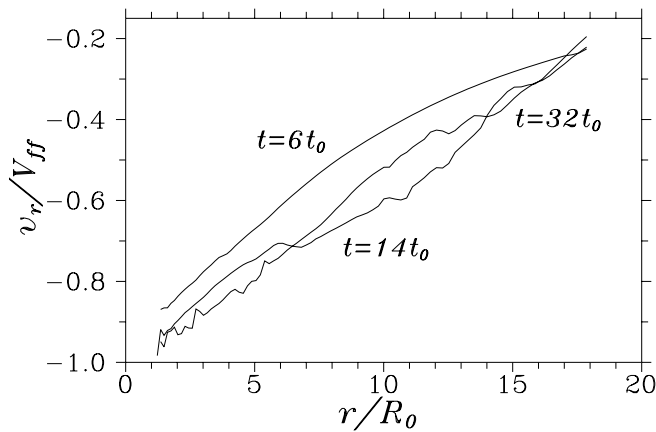


FIG. 7.—Variation of radial velocity  $v_r$  with  $r$  in the midplane of the disk at times  $t = 6t_0$ ,  $14t_0$ , and  $32t_0$ , where  $t_0$  is the rotation period at the inner radius of the disk.

Note, that for  $r \sim R_0$ , the radial inflow velocity is close to the free-fall velocity  $V_{ff} = \sqrt{2GM/R}$ . An inflow velocity  $\sim \sqrt{GM/R}$  is predicted by LC. Velocity is strongly supersonic with Mach number  $M > 100$ . Figure 7 shows that velocity distribution along the disk is almost the same during the long time. Figure 8 shows the dependence of density on radial distance.

The density of the disk decreases with time, specifically in the inner regions of the disk. Both the velocity and density show small-scale wavelike variations as a function of radius.

Figure 9 shows the observed vertical ( $z$ ) variation of the radial and azimuthal velocities in the disk at  $r = 7R_0$  and the theoretical dependencies calculated by LC. The dimensionless vertical length  $\zeta$  was introduced by LC as  $\zeta = z/h$ , where  $h = h(r)$  is the characteristic half-thickness of the boundary layer in which most of the radial inflow of matter occurs. Consistent with LC, we find that  $(h/H)^2 \ll 1$  over most of the disk surface, where  $H$  is the full disk half-thickness. At  $r = 7R_0$ , we find  $h/H \approx 0.25$ . One can see that radial inflow velocity has a maximum in the midplane of the disk and decreases to small values at large  $\zeta$ . Note that we observe weak outflows for  $4 < \zeta < 8$  where  $v_r > 0$ . Similar outflows were predicted by LC (solid curves). The azimuthal velocity  $v_\phi$  grows with increasing  $\zeta$  and reaches the Keplerian velocity for  $\zeta \lesssim 2.4$ . There is also a region where the azimuthal velocity is slightly larger than Keplerian

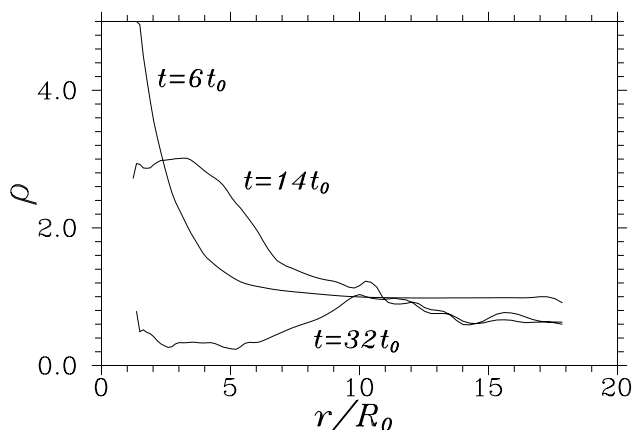


FIG. 8.—Variation of density with  $r$  in the midplane of the disk at the same time intervals as Fig. 7.

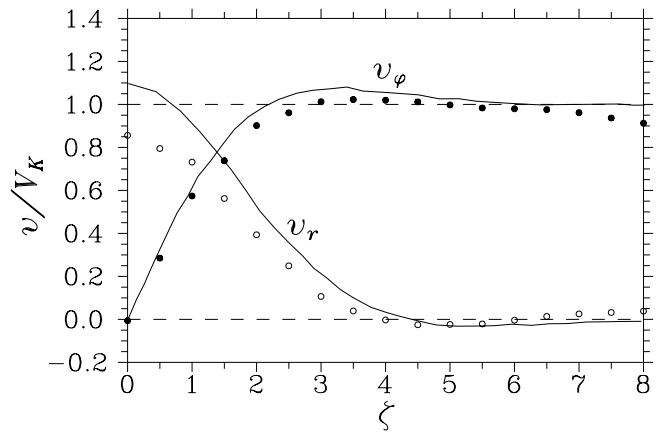


FIG. 9.—Radial velocity  $v_r$  (open circles) and azimuthal velocity  $v_\phi$  (filled circles) velocities across the disk as a function of  $\zeta \equiv z/h$  at radial distance  $r = 7R_0$ . Here  $h(r)$  is the characteristic half-thickness of the region of the strongest inflow, and  $V_K \equiv \sqrt{GM/r}$ . The solid lines show the theoretical dependences from LC. Note that to a good approximation  $v_r$  is an even function of  $\zeta$  and  $v_\phi$  is an odd function.

velocity,  $3 < \zeta < 4.5$ . A similar region was predicted by LC (see solid curve in Fig. 9).

The conditions considered by LC were different from the initial conditions considered for our simulations. Thus, it appears that the main features of vertically stratified counterrotating flows do not depend strongly on the initial conditions. At longer times in our simulation runs, the region of fast equatorial flow becomes somewhat thicker. Overall the simulation results are close to the predictions of the analytic model of LC. Although the analytic model includes viscous heating and radiative cooling, these almost compensate each other with the result that the model is close to the simulations, which have almost isothermal conditions and no radiative cooling.

Figure 10 shows the radial dependence of the mass accretion rate  $\dot{M}(r)$  at different times and that for a disk rotating in one direction at time  $t = 40t_0$  (§ 3.1). The mass accretion rate for the counterrotating disk can be written as

$$\dot{M} \approx 2\pi r \rho(r, z=0) V_K(r) [3.25h(r)] \quad (7)$$

where the numerical coefficient (3.25) is obtained from Figure 9. In that the surface mass density of the disk is

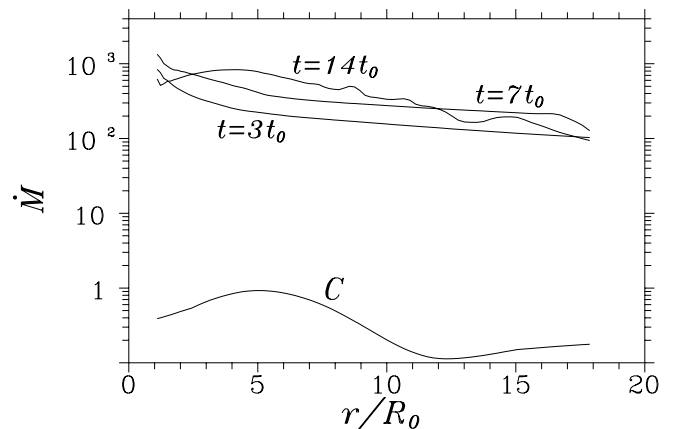


FIG. 10.—Mass accretion rate as a function of radial distance  $r$  at different moments of time. The upper curves are for a counterrotating disk at times  $t = 3t_0$ ,  $7t_0$ , and  $14t_0$ . The lower curve (C) is for a conventional accretion disk rotating in one direction at time  $t = 40t_0$ , where the accretion results from the numerical viscosity of the code.

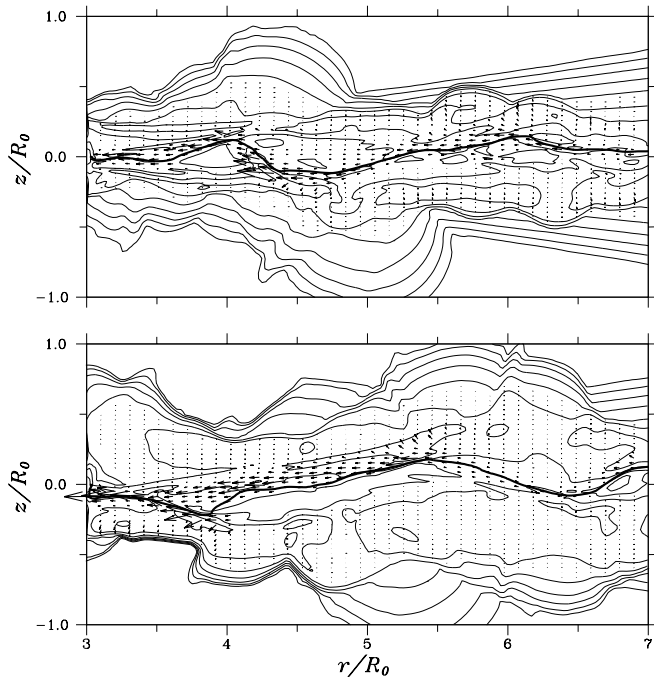


FIG. 11.—Contours of density and velocity vectors for  $\gamma = 1.1$  at times  $t = 4.8t_0$  (bottom panel) and  $t = 6.2t_0$  (top panel). The heavy line separates the corotating and counterrotating gas. The simulations were performed for the part of the disk  $3 \leq r/R_0 \leq 7$  with a  $200 \times 200$  grid.

$\Sigma = 2\pi\rho(r, z = 0)2H$ , the average accretion speed is  $u_{\text{CR}} \approx 1.62(h/H)V_K$ . For comparison, the mass accretion rate for a conventional  $\alpha$ -disk rotating in one direction (Shakura 1973; Shakura & Sunyaev 1973) is

$$\dot{M}_{\text{SS}} \approx 2\pi r \rho(r, z = 0) V_K(r) \left( \frac{\alpha c_s^2}{V_K^2} \right) 2H(r). \quad (8)$$

In this case the average accretion speed is  $u_{\text{SS}} = \alpha(c_s/V_K)^2 V_K$ . For a conventional accretion disk, the quantity  $\alpha(c_s/V_K)^2$  is commonly thought to be much smaller than unity. For example, for  $c_s/V_K = 0.01$ ,  $h/H = 0.1$ , and  $\alpha = 0.1$ ,  $\dot{M}/\dot{M}_{\text{SS}} \approx 1.6 \times 10^4$ .

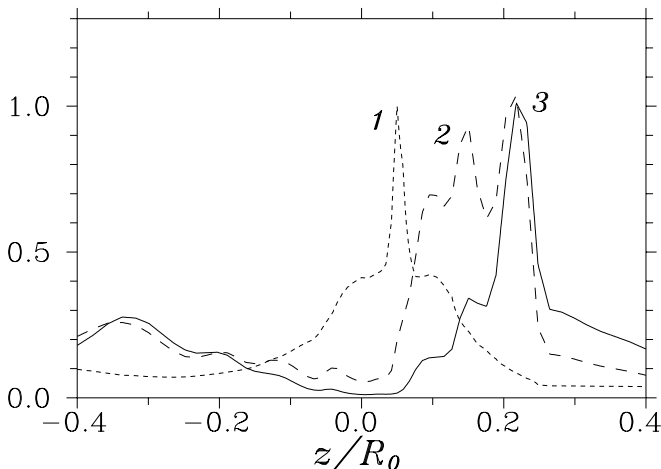


FIG. 12.—Profiles of the (1) density, (2) pressure, and (3) temperature through the disk at  $r = 5R_0$  at the time  $t = 6.2t_0$  corresponding to the top panel of Fig. 11.

### 3.3. $\gamma = 1.1$ and $\gamma = 5/3$

We also did simulations of vertically stratified counterrotating disks for  $\gamma = 1.1$  and  $\gamma = 5/3$ , which correspond to nonisothermal conditions where the effect of viscous heating is more important. We find in general that after a given time and for a given numerical grid, the temperatures in the disk increase as  $\gamma - 1$  increases. Thus, the disk thickness  $H/r$  is larger for larger  $\gamma - 1$ . On the other hand, for fixed  $\gamma$ , the temperature in the disk decreases gradually as the resolution  $N_R \times N_\theta$  increases. Here we performed simulations with the  $200 \times 200$  grid. To increase the resolution even more (to decrease viscosity), we performed simulations of only part of the disk:  $3R_0 < r < 7R_0$ .

At early times ( $t/t_0 \sim 1-3$ ), the flow in the equatorial plane of the disk was similar to that for  $\gamma = 1.01$ . However, for longer times, the region of fast poloidal inflow begins to warp. Figure 11 shows contours of density and velocity vectors of the disk at two times. The amplitude of the warp of the interface  $\Delta z$  between corotating and counterrotating flows grows. After a fixed time the warp amplitude is a strongly increasing function of  $\gamma - 1$ . For  $\gamma = 1.01$  the fractional warp amplitude  $\Delta z/r$  is very small for all times. However, the warp amplitude for  $\gamma = 1.1$  is  $\Delta z/r \approx 0.034$ , and for  $\gamma = 5/3$  it is  $\Delta z/r \approx 0.13$ , both at  $t/t_0 = 7$  with the same resolution as used in Figure 11. The warp amplitude  $\Delta z$  is of the order of the disk half-thickness  $H$ . For  $\gamma = 1.1$  the dominant radial wavelength is  $\lambda_r \sim 1.5R_0$  whereas for  $\gamma = 5/3$  there is a wide spectrum of wavelengths from  $\sim R_0$  to  $\ll R_0$ . The warping is suppressed by low grid resolution.

The warping may represent a Kelvin-Helmholtz type of instability driven by the shear in the poloidal flow. The tidal gravitational force of the central object,  $F_z$ , acts to keep the warp amplitude from growing without bound. Note that Kelvin-Helmholtz instabilities driven by the shear in the azimuthal flow are suppressed in our simulations which are axisymmetric. Alternatively, the disk warping may be due to unsymmetrical (top/bottom) heating of the disk that gives an excess pressure in, say, the bottom half of the disk, which displaces the disk upward. Plots of the pressure, density, and temperature through the disk as shown in Figure 12 support this simple explanation.

### 4. DISK COUNTERROTATING IN THE $r$ -DIRECTION: MODEL II

Here we treat model II, which is shown schematically in the middle panel of Figure 1. In this model the inner part of the Keplerian disk ( $r < r_t$ ) rotates in the positive direction whereas the outer part ( $r > r_t$ ) rotates in the opposite direction. The transition between positive and negative azimuthal velocity was centered at  $r/R_0 = 14$  and extended over the narrow region  $13.5 < r/R_0 < 14.5$ . This transition region is small, involving only five grid points in the radial direction for a mesh size of  $100 \times 100$ . The boundary condition at the right side of the disk was taken the same as in model I. Simulations were performed for  $\gamma = 1.1$  and  $\gamma = 5/3$ . Results are presented for  $\gamma = 1.1$ .

In our simulations, matter in the transition zone with low angular momentum flows rapidly inward, compressing matter at smaller radii as shown in Figures 13 and 14. This inflow sets up a density wave that propagates inward in the disk. The matter behind the wave has lower density. The speed of propagation of the wave grows with time and reaches a maximum value equal to about one-half of the

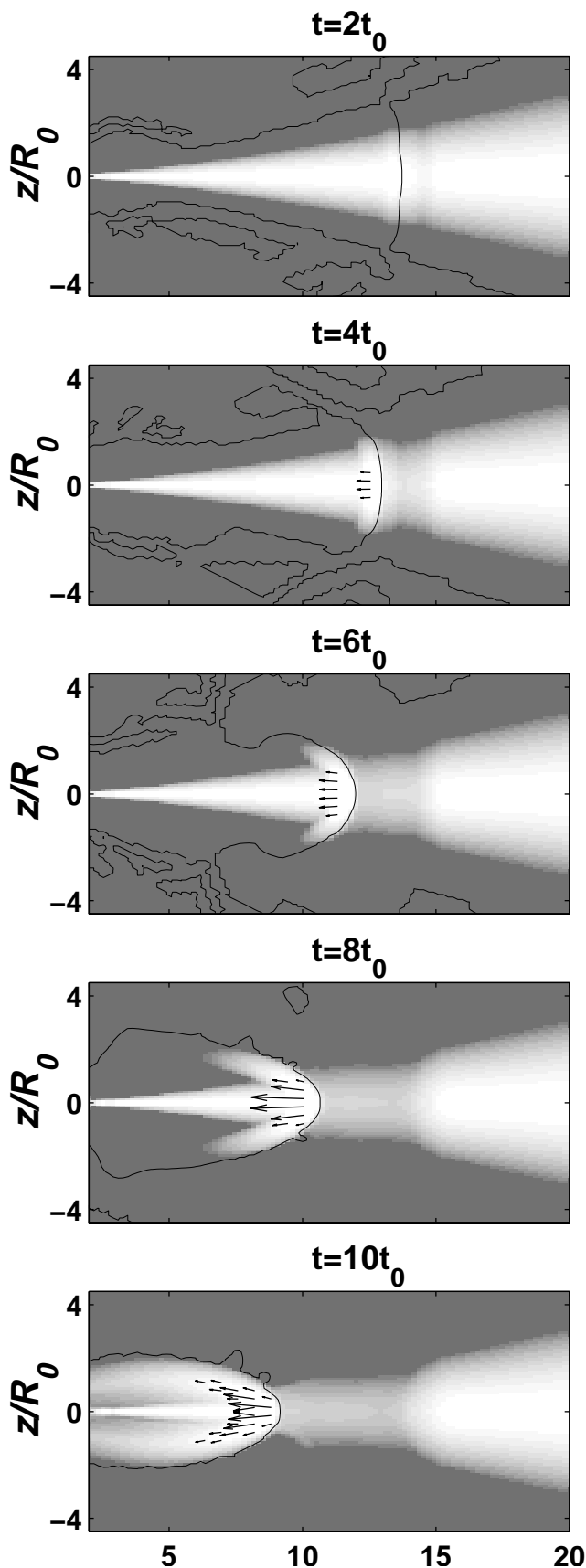


FIG. 13.—Gray-scale plots of density and matter flux vectors showing the evolution of model II. Starting from the top, the panels show times  $t = 2t_0, 4t_0, 6t_0, 8t_0,$  and  $10t_0$ . The vectors are proportional to the value of the mass flux  $\rho v$ . The black solid line shows the line of zero azimuthal velocity. For the case shown,  $\gamma = 1.1$ .

free-fall velocity (see Fig. 14). The azimuthal velocity in the wave is sub-Keplerian with  $v_\phi \sim (0.6\text{--}0.8)v_K$  in the inner part of the disk. Matter behind the wave (at larger  $r$ ) has opposite velocity, with a magnitude somewhat smaller than the local Keplerian velocity (see Fig. 14). The wave propagates supersonically, with Mach number  $M \sim 20\text{--}30$ . The Mach number grows as the wave moves inward (see Fig. 14).

The shock wave propagating initially at times  $t < 10t_0$  is not a standard shock wave, because it has significant angular momentum, and its formation and propagation is based on the deficit of angular momentum of the matter of the wave and an imbalance of gravitational and centrifugal forces. The density and velocity jumps are much larger than in the case of standard shock wave (see Fig. 14). This wave resembles a soliton-type wave. A similar type of wave was observed in accretion disks where a local deficit of angular momentum was caused by magnetically driven outflows (Lovelace, Romanova, & Newman 1994; Lovelace, Newman, & Romanova 1997). Note that the solid line in Figure 13 indicates the boundary between corotating and counterrotating components. The density wave reaches  $r = 8R_0$  during  $t = 10t_0$  (10 periods of rotation of the inner edge of the disk). For longer times, matter started to “reflect” from the inner regions and move outward.

The effective collapse of the inner disk can be understood by considering the details of the model used. The density of the disk is constant along the equatorial plane so that the mass of the equidistant rings  $\Delta R = \text{const}$  increases outward,  $\Delta M = 2\pi\rho r\Delta r \sim r$ , so that the mass of ring at  $r = 14$  is 14 times larger than a ring at  $r = 1$ . At the same time, the angular momentum of the rings increases outward as  $\Delta L \sim \Delta M v_K r \sim r^{3/2}$ , so that the angular momentum of inner ring is 52 times smaller than of the ring at  $r = 14$ . The layer between counterrotating disks has pretty large mass and zero angular momentum. It is not centrifugally supported and falls down to the center. It accumulates the matter of the inner regions of the disk and their angular momentum. But absorbed angular momentum is not sufficient to reach the centrifugal barrier.

The thickness of the boundary layer in which there is annihilation of angular momentum depends on the viscosity. For a larger viscosity, the layer is thicker and the propagating wave is stronger. The fast inward propagation of such a wave in a disk around a black hole would give an outburst in the luminosity as the wave reaches the black hole. This represents a possible mechanism of generating outbursts in active galactic nuclei, for example.

#### 5. INFLOW OF COUNTERROTATING GAS ONTO A COROTATING DISK: MODEL III

Here we discuss model III, which is shown schematically in the bottom panel of Figure 1. In this case counterrotating gas of relatively low density inflows with significant poloidal speed and encounters an existing Keplerian disk. For the simulations, we took Initial Conditions 2 (§ 2.4.2) corresponding to a finite radius, slightly sub-Keplerian, corotating disk (see Fig. 3). The effective outer radius of this disk was taken to be at  $r_{\text{out}} = 11.5R_0$ . At the outer, right-hand boundary of the computational region, matter is launched into the simulation region from the part of the boundary  $-3 < z/R_0 < 3$  with radial velocity  $v_r = 0.7V_K$  and azimuthal velocity  $v_\phi = -V_K$ . When both the “target” disk and incoming matter rotate in the same direction, then

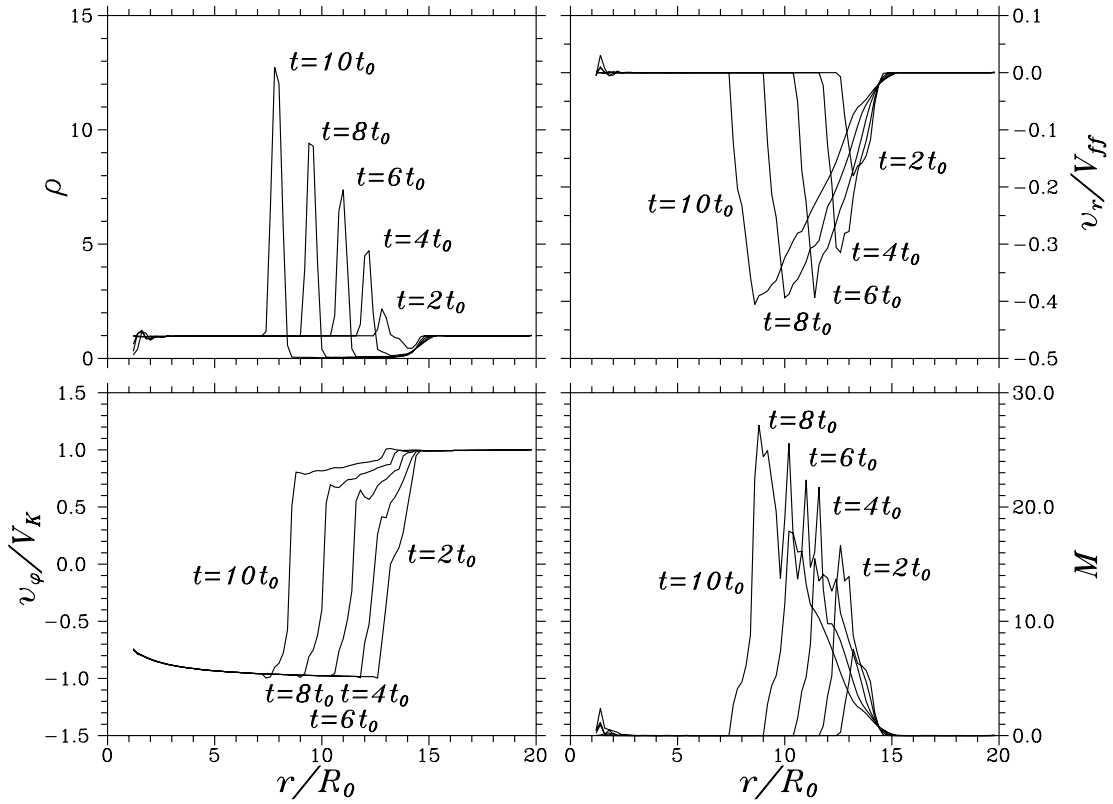


FIG. 14.—Radial distributions of density (*top left panel*), radial velocity (in units of local free-fall velocity) (*top right panel*), azimuthal velocity (in units of local Keplerian velocity) (*bottom left panel*), and Mach number (*right bottom panel*) at different times,  $t = 2t_0, 4t_0, 6t_0, 8t_0$ , and  $10t_0$ . The time sequence corresponds to that shown in Fig. 13.

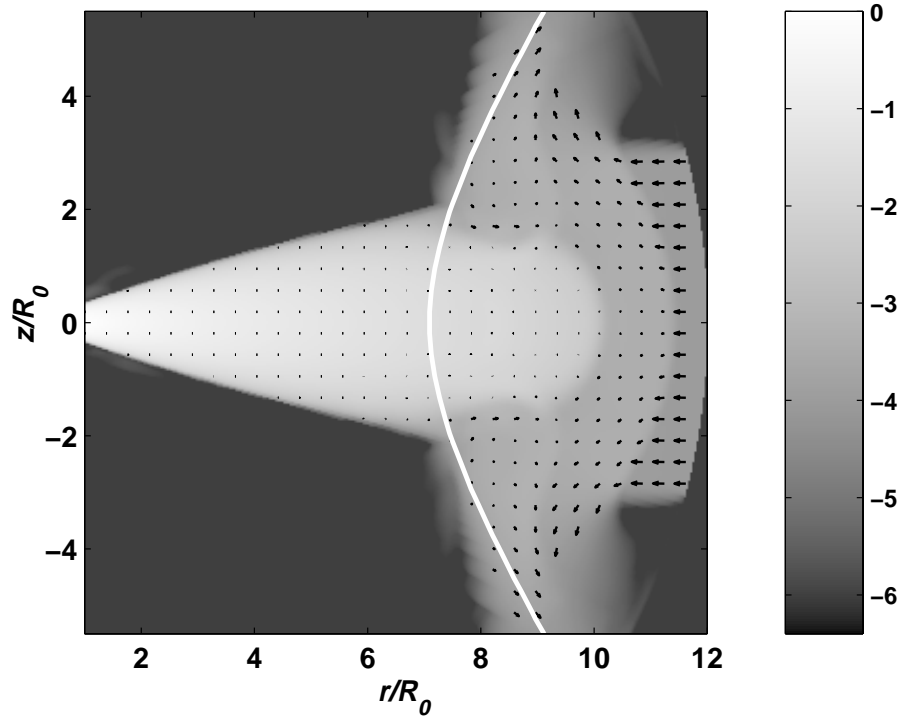


FIG. 15.—Results of simulations of model III where radially inflowing matter encounters an existing corotating disk. The inflowing matter rotates in the same direction as the disk and there is no accretion. The inflowing matter is injected at  $z \sim \pm 3R_0$ . The logarithm of the density is represented by the gray scale shown. The white line shows centrifugal barrier for the inflowing gas. The vectors show the poloidal velocity. The plot is for  $t = 20t_0$ . Simulations were performed with resolution  $N_r = 150$  and  $N_\theta = 100$ .

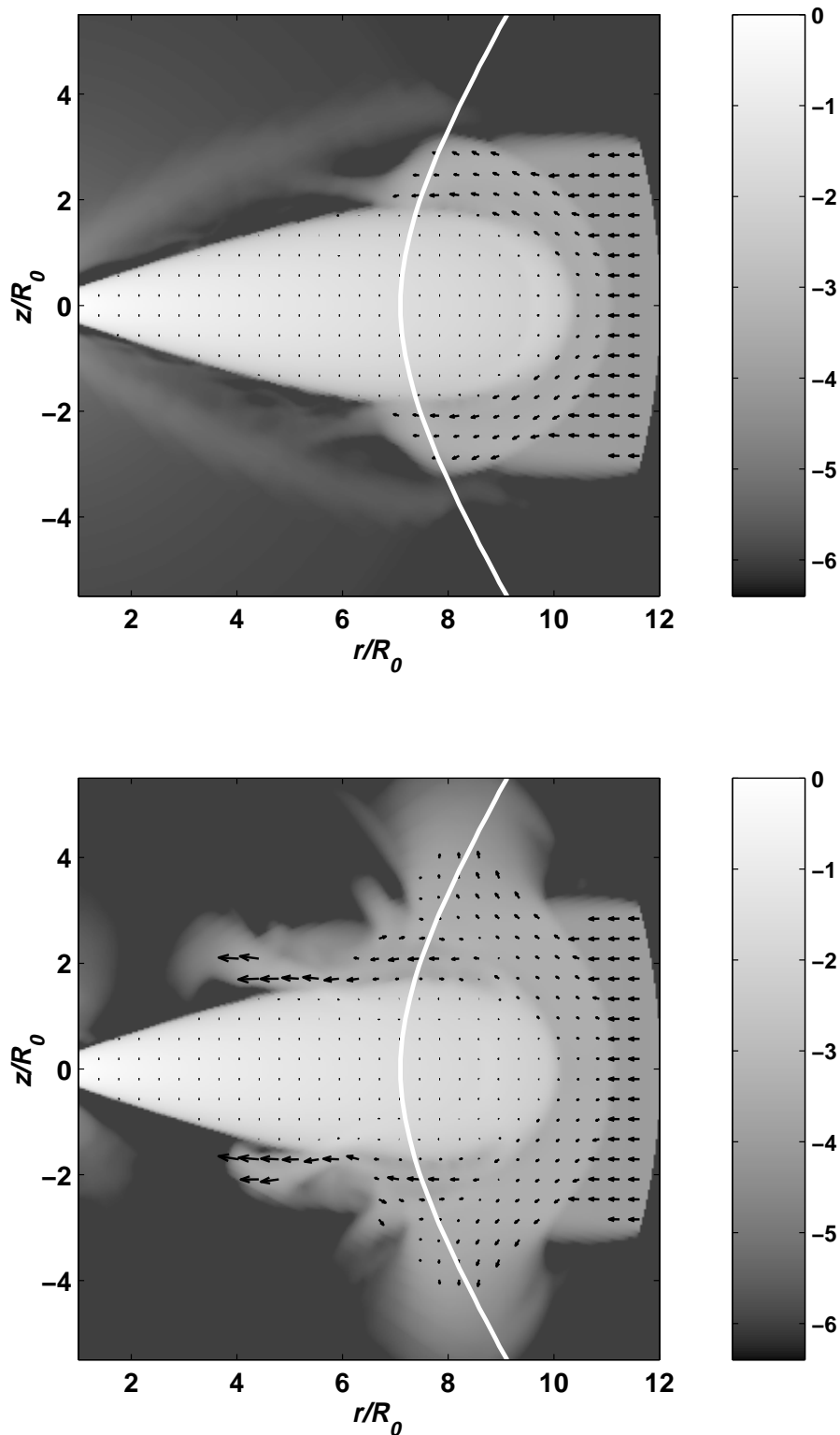


FIG. 16.—Results of simulations of model III for the case where the inflowing matter rotates in the *opposite* direction to that of the disk. In this case, incoming counterrotating matter interacts strongly with the main disk. The resulting low angular momentum gas starts to accrete rapidly along the surfaces of the disk. The times  $t = 4.5t_0$  (*top panel*) and  $7t_0$  (*bottom panel*) of evolution are shown. The logarithm of the density is represented by the gray scale shown. The white lines in both panels show centrifugal barrier for the inflowing gas. The vectors show the poloidal velocity.

incoming matter moves inward only until it reaches the centrifugal barrier (see white line on Fig. 15), then it stops, and moves in the  $\pm z$ -directions away from the disk surface.

Figure 15 shows the observed behavior of density and velocity in this case. Note, that in this case we observe only very small accretion connected with finite viscosity of the disk. This case was considered for reference.

When the inflowing matter rotates in the *opposite* direction to that of the “target” disk, then it also reaches a centrifugal barrier. However, a nonnegligible fraction  $f$  of the inflowing matter interacts with the disk, causing angular momentum annihilation. For this case, the fraction is  $f \sim 0.2$ . Figures 16 and 17 show the evolution. One can see from Figure 16 (*top and bottom panels*) that at times  $3 <$

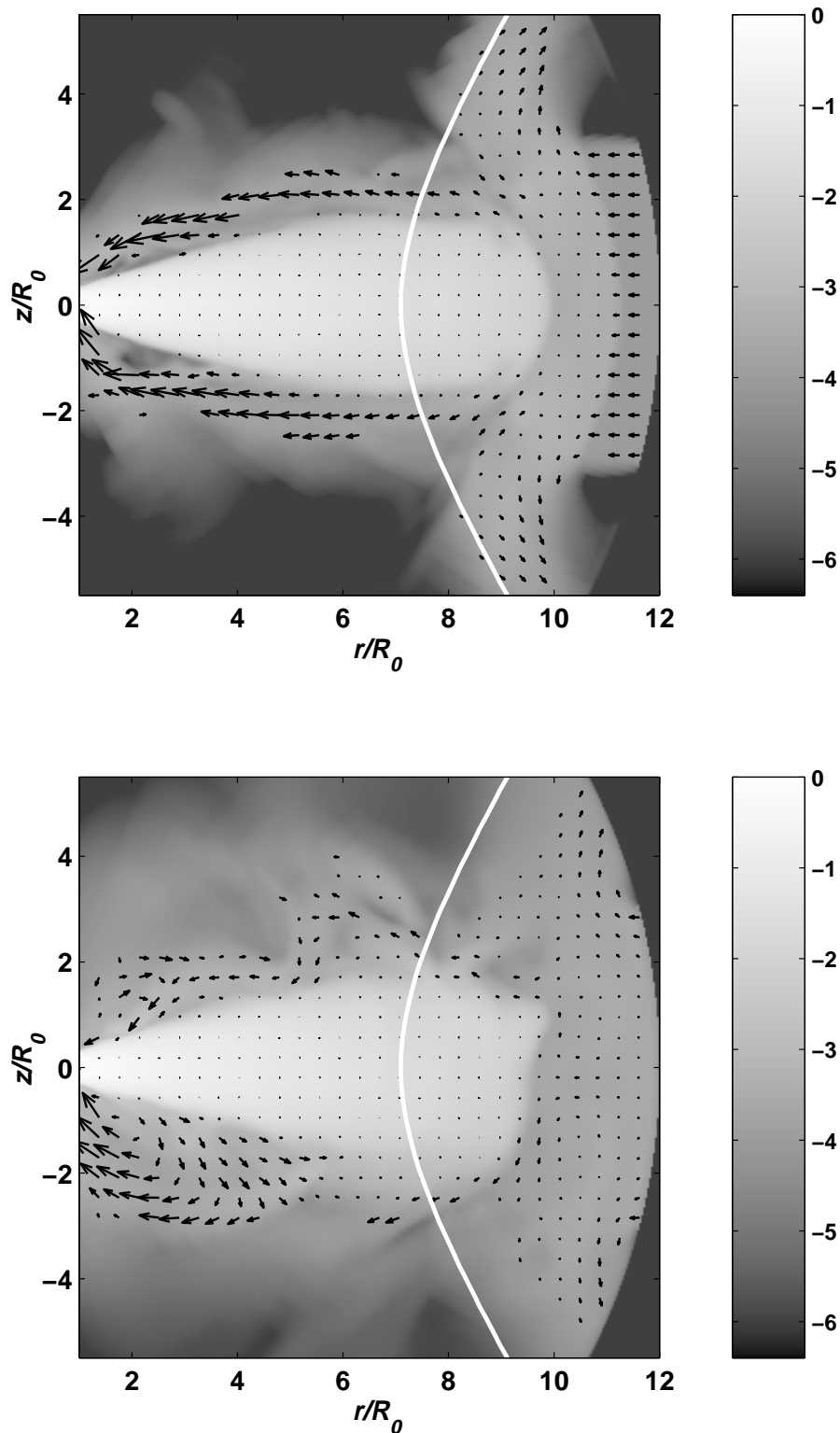


FIG. 17.—Continuation of Fig. 16. The top panel is for  $t = 20t_0$ , when the surface layer accretion is strong. The bottom panel is for  $t = 35t_0$ , when the surface accretion is destroyed by the dissipative heating.

$t/t_0 < 7$ , the gas starts to flow along the surfaces of the target disk. Later, at  $7.5 < t/t_0 < 15$ , it flows strongly along the surfaces (see top panel of Fig. 17). The radial velocity of matter flowing along the surfaces is  $\sim (0.3-0.5)V_{ff}$ . Later, the layer became thicker owing to viscous dissipation and the flow became more chaotic (Fig. 17, bottom panel). The temperatures increased few times in the surface layer. Here we should remember that viscous heating is included, but

cooling is not. If radiative cooling balances viscous heating, then this surface layer may survive much longer than in the simulation. The surface flow is similar in some respects to that observed in model I (§ 3). As in model I, we also observed the increase of the radial inflow velocity with decreasing  $r$ .

In this model, we also observed an interaction similar to that investigated in model II. Namely, the interaction

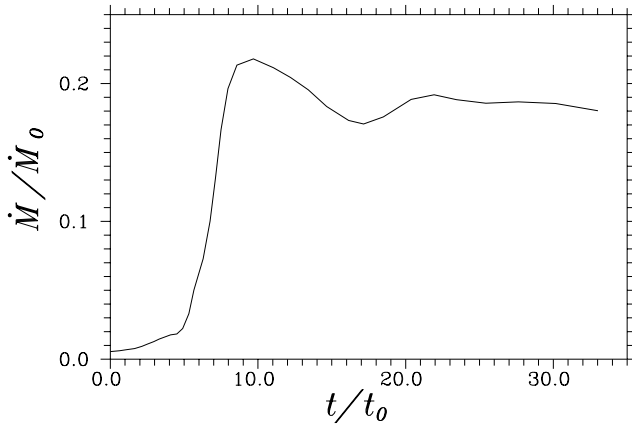


FIG. 18.—Matter flux through the cylindrical surface  $r = 5R_0$  in model III. It has a peak owing to the surface accretion, then is almost constant owing to both surface accretion and enhanced accretion inside the main disk.

occurred not only along the surfaces of the disk but also through the cross section of the disk. As a result, accretion was enhanced inside the main disk as in model II. Compared with model II, the density of counterrotating matter is much smaller than that of the “target” disk. For this reason, the interaction did not lead to dramatic wave formation. The radial velocity of viscous flow inside the disk increased by a factor of  $\sim 50$ , and matter flux increased by a similar factor. However, the velocity of accretion of the main disk remained much smaller than the free-fall velocity.

Note that during this violent evolution of the outer layers of the disk, the main part of the “target” disk was very stable, the density did not change appreciably, and the radial velocities remained small.

Figure 18 shows the time evolution of the matter flux through the cylindrical surface  $r = 5R_0$ . It increases by a factor  $\sim 50$  compared with the initial flux. For  $t/t_0 \lesssim 10$ , it increases mainly as a result of surface layer accretion. Later, there is also enhanced accretion from the main part of the “target” disk. A fraction about  $\sim 0.2$  of the incoming matter is accreted.

## 6. TWO APPLICATIONS

Here we briefly consider two applications of our results to accretion disks. One is related to galaxies and the second to X-ray pulsars.

### 6.1. Galaxies

In some disk galaxies, counterrotating gas and/or stars are observed (e.g., Rubin 1994a, 1994b; Galletta 1995). Even though the present work treats Keplerian disks, we can nevertheless make estimates based on our hydrodynamic results. The rotation curves of galactic disks are flat ( $v_\phi = \text{const}$ ) over a significant range of distances owing in part to a spheroidal distribution ( $\rho \propto r^{-2}$ ) of dark matter. Although this rotation curve is quite different from Keplerian, the analytic viscous accretion flows are nearly the same for flat and Keplerian rotation curves (LC). The reason is that the boundary layer formed between the oppositely rotating components, where angular momentum is annihilated and fast accretion occurs, does not depend strongly on the radial dependence of  $v_\phi$ .

We consider the situation where a counterrotating cloud of hydrogen of mass  $M_{\text{cl}} = 10^9 M_\odot$  is captured into an equatorial orbit of radius  $r_{\text{out}} = 20 \text{ kpc}$ . Model III is perti-

nent to this situation. Interaction between the counterrotating cloud and existing corotating gas (assumed mass  $\geq M_{\text{cl}}$ ) in the galaxy leads to fast boundary layer accretion along the top and bottom surfaces of the galactic disk with average accretion speed  $u_{\text{CR}} \sim 3.25(h/H)V_c$ , where we have adapted the results of § 3 to model III, which has two boundary layers, and where we have used the circular velocity of the galaxy  $V_c \approx \text{const}$  rather than the Keplerian velocity  $V_K$ . The timescale for this fast accretion to the center of the galaxy is therefore

$$t_{\text{CR}} \sim \frac{r_{\text{out}}}{u_{\text{CR}}} \sim 3 \times 10^8 \text{ yr} \left( \frac{r_{\text{out}}}{20 \text{ kpc}} \right) \left( \frac{200 \text{ km s}^{-1}}{V_c} \right), \quad (9a)$$

where we have assumed  $h/H = \text{const} = 0.1$ . For the reference values of equation (9a) and assuming that the cloud mass is accreted in a time  $\sim 10t_{\text{CR}}$ , the mass accretion rate is

$$\dot{M} \sim \frac{2M_{\text{cl}}}{10t_{\text{CR}}} \sim 0.6 M_\odot \text{ yr}^{-1}, \quad (9b)$$

where the factor of 2 accounts for the fact that half of the accreted gas is from the existing disk. Note that the accretion timescale is much less than the Hubble time.

### 6.2. X-Ray Pulsars

Nelson et al. (1997a, 1997b) and Chakrabarty et al. (1997) have proposed that the change from spin-up to spin-down of X-ray pulsars in binary systems results from a reversal of the angular momentum of the wind supplied accreting matter. The matter inflowing to the pulsar is assumed to be supplied at a constant rate  $\dot{M}$  at a radius  $r_{\text{out}}$  in the equatorial plane of the binary system. Initially, the pulsar is assumed to have a conventional, corotating disk. Then, due to some disturbance, the direction of rotation of the supplied matter reverses so that it is counterrotating. Model III is again pertinent to this situation. The “new” counterrotating matter encounters the “old” corotating disk. Interaction between the “new” and “old” matter leads to fast boundary layer accretion with average accretion speed  $u_{\text{CR}} \sim 3.25(h/H)V_K$ . The timescale for this fast accretion to reach the pulsar is

$$t_{\text{CR}} = \int_0^{r_{\text{out}}} \frac{dr}{u_{\text{CR}}} \sim 2 \text{ days} \left( \frac{M_\odot}{M} \right)^{1/2} \left( \frac{r_{\text{out}}}{10^{12} \text{ cm}} \right)^{3/2}, \quad (10)$$

where we have again assumed  $h/H = \text{const} = 0.1$ . The sign of the angular momentum carried by the boundary layer flows at the much smaller Alfvén radius  $r_A \ll r_{\text{out}}$ , which determines the spin-up or spin-down of the pulsar, is uncertain from the present work. If this has the sense of the counterrotating material supplied at  $r_{\text{out}}$ , then a rapid switch between spin-up and spin-down of the pulsar would occur with timescale of order  $t_{\text{CR}} \sim \text{days}$ .

On a much longer timescale, inflowing counterrotating matter will “use up” the old corotating disk. This timescale is simply the accretion time for a disk rotating in one direction,

$$t_{\text{SS}} = \int_0^{r_{\text{out}}} \frac{dr}{u_{\text{SS}}} \sim 0.7 \times 10^5 \text{ days} \times \left( \frac{0.1}{\alpha} \right) \left( \frac{0.01}{c_s/V_K} \right)^2 \left( \frac{M_\odot}{M} \right)^{1/2} \left( \frac{r_{\text{out}}}{10^{12} \text{ cm}} \right)^{3/2}. \quad (11)$$

A further time interval  $\sim t_{\text{SS}}$  is required for establishment of an equilibrium  $\alpha$ -disk rotating in the opposite direction to the original disk.

## 7. CONCLUSIONS

Time-dependent, axisymmetric hydrodynamic simulations have been used to study Keplerian accretion disks consisting of counterrotating components. The simulation code used for the study has a numerical viscosity that is calibrated by the study of the accretion of a disk rotating in one direction. Different grid resolutions were used to study the influence of the numerical viscosity. Our simulation model does not include radiative cooling. Therefore, different values of the specific heat ratio  $\gamma$  from 1.01 to 5/3 were used in order to assess the influence of heating due to the numerical viscosity. A small value of  $\gamma - 1$  corresponds to almost isothermal conditions.

Different cases were considered. In model I, the gas well above the disk midplane rotates in one direction and that well below has the same properties but rotates in the opposite direction. In this case, there is angular momentum annihilation in a narrow equatorial boundary layer in which matter accretes supersonically with a velocity that approaches the free-fall velocity. The average accretion speed of the disk can be enormously larger than that for a conventional  $\alpha$ -viscosity disk rotating in one direction. For a much lower viscosity (when we took a small part of the region and calculated it with a grid resolution of  $200 \times 200$ ), the interface between the corotating and counterrotating components shows significant warping, which is probably a type of Kelvin-Helmholtz instability. We observed that a large viscosity suppresses this instability.

In model II, we considered the case where the inner part of the disk corotates while the outer part counterrotates. In this case a new equilibrium inner disk forms with a low-density gap between inner and outer disks. In model III we investigated the case where low-density counterrotating matter inflowing from large radial distances encounters an existing corotating disk. Friction between the inflowing matter and the existing disk is found to lead to fast boundary layer accretion along the disk surfaces, whereas interaction of the disk with counterrotating matter at large radii leads to enhanced accretion in the main body of the disk. We observed that the boundary layer accretion is a temporary phenomenon, because the interaction of the dense disk and low-density counterrotating gas leads to heating of this

gas. However, the interaction at large radii is more steady and leads to continuous enhanced accretion in the main disk.

These models are pertinent to the formation of counterrotating disks in galaxies, in active galactic nuclei, and in X-ray pulsars in binary systems. For galaxies, the high accretion speed allows counterrotating gas to be transported into the central regions of a galaxy in a time much less than the Hubble time.

It is clear that inclusion of the important role of Kelvin-Helmholtz (KH) instabilities in counterrotating disks requires three-dimensional simulations, and this will be the subject of a future paper. For example, note that in model I if the flow is treated as a vortex sheet without radial inflow, then a local stability analysis  $k^2 H^2 \geq 1$ , with  $k$  the  $(r, \phi)$  wavevector, indicates unstable KH warping for wavenumbers  $|k_\phi/k_r| < \sqrt{2}(c_s/V_K) \ll 1$  and a maximum growth rate of  $|k_r|c_s/2$  (LC; Choudhury & Lovelace 1986). To account for this nonaxisymmetric warping instability of the disk, we clearly need three-dimensional simulations. In model II, a local stability analysis of the interface between the inner and outer disks indicates unstable KH warping for  $|k_\phi/k_z| < \sqrt{2}c_s/V_K \ll 1$  and a maximum growth rate of  $|k_z|c_s/2$ . Also, in this case, three-dimensional simulations are needed.

A number of further developments are planned. Simulations explicitly including an  $\alpha$ -viscosity are desirable for detailed comparison with theory. Explicit inclusion of radiative cooling is equally important. Also, three-dimensional simulations are needed to investigate the Kelvin-Helmholtz instability.

One of the authors (M. M. R.) thanks R. Giovannelli and D. Dale for helpful discussions. We thank an anonymous referee for many constructive comments on an earlier version of this work. This work was supported in part by NSF grant AST 93-20068. O. A. K. and V. M. C. were supported in part by the Russian Federal Program "Astronomy" (subdivision "Numerical Astrophysics") and by INTAS grant 93-93-EXT. Also, this work was made possible in part by grant RP1-173 of the US Civilian R&D Foundation for the Independent States of the Former Soviet Union. The work of R. V. E. L. was also supported in part by NASA grant NAG 5-6311.

## REFERENCES

- Abakumov, M. V., Mukhin, S. I., Popov, Yu. P., & Chechetkin, V. M. 1996, *Astron. Rep.*, 40, 366  
 Barnes, J. E. 1992, *ApJ*, 393, 484  
 Bisikalo, D. V., Boyarchuk, A. A., Kuznetsov, O. A., & Chechetkin, V. M. 1996, *Astron. Rep.*, 40, 662  
 Blondin, J. M., Kallman, T. R., Fryxell, B. A., & Taam, R. E. 1990, *ApJ*, 356, 591  
 Braun, R., Walterbos, R. A. M., Kennicutt, R. C., Jr., & Tacconi, L. J. 1994, *ApJ*, 420, 558  
 Chakrabarty, D., et al. 1997, *ApJ*, 481, L101  
 Chakravarthy, S., & Osher, S. 1985, A New Class of High Accuracy TVD Schemes for Hyperbolic Conservation Laws (AIAA Paper 85-0363)  
 Choudhury, S. R., & Lovelace, R. V. E. 1986, *ApJ*, 302, 188  
 Davies, C. L., & Hunter, J. H., Jr. 1997, *ApJ*, 484, 79  
 Falcke, H., & Melia, F. 1997, *ApJ*, 479, 740  
 Galletta, G. 1995, in *ASP Conf. Ser. 91, Barred Galaxies*, ed. R. Buta, D. Crocker, & B. Elmegreen (San Francisco: ASP), 429  
 Hernquist, L. E., & Barnes, J. E. 1991, *Nature*, 354, 210  
 Khokhlov, A., & Melia, F. 1996, *ApJ*, 457, L61  
 Livio, M., Soker, N., Matsuda, T., & Anzer, U. 1991, *MNRAS*, 253, 633  
 Lovelace, R. V. E., & Chou, T. 1996, *ApJ*, 468, L25 (LC)  
 Lovelace, R. V. E., Jore, K. P., & Haynes, M. P. 1997, *ApJ*, 475, 83  
 Lovelace, R. V. E., Newman, W. I., & Romanova, M. M. 1997, *ApJ*, 484, 628  
 Lovelace, R. V. E., Romanova, M. M., & Bisnovaty-Kogan, G. S. 1998, *ApJL*, submitted  
 Lovelace, R. V. E., Romanova, M. M., & Newman, W. I. 1994, *ApJ*, 437, 136  
 Melia, F. 1994, *ApJ*, 426, 577  
 Moderski, R., & Sikora, M. 1996, *A&AS*, 120C, 591  
 Nelson, R. W., et al. 1997a, in *ASP Conf. Ser. 121, Accretion Phenomena and Related Outflows*, ed. G. Bicknell, L. Ferrario, & D. Wickramasinghe (San Francisco: ASP), 256  
 ———. 1997b, *ApJ*, 488, L117  
 Rees, M. J. 1990, *Science*, 247, 817  
 Rubin, V. C. 1994a, *AJ*, 107, 173  
 ———. 1994b, *AJ*, 108, 456  
 Rubin, V. C., Graham, J. A., & Kenney, J. D. P. 1992, *ApJ*, 394, L9  
 Ruffert, M. 1994, *ApJ*, 427, 342  
 Ruffert, M., & Melia, F. 1994, *A&A*, 288, L29  
 Sawada, K., & Matsuda, T. 1992, *MNRAS*, 255, 17P  
 Sawada, K., Matsuda, T., & Hachisu, I. 1986, *MNRAS*, 219, 75  
 Shakura, N. I. 1973, *Soviet Astron.*, 16, 756  
 Shakura, N. I., & Sunyaev, R. A. 1973, *A&A*, 24, 337  
 Shlosman, I., Begelman, M. C., & Frank, J. 1990, *Nature*, 345, 679  
 Thakar, A. R., & Ryden, B. S. 1996, *ApJ*, 461, 55  
 Vyaznikov, K. V., Tishkin, V. V., & Favorsky, A. P. 1989, *Math. Modeling*, 1, 79 (in Russian)